PERGAMON

International Journal of Heat and Mass Transfer 42 (1999) 1665–1688

International Journal of HEAT and MASS TRANSFER

Orientation effects on pool boiling critical heat flux (CHF) and modeling of CHF for near-vertical surfaces

Alicia H. Howard[1], Issam Mudawar*,[2]

Boiling and Two-phase Flow Laboratory, School of Mechanical Engineering, Purdue University, West Lafayette, IN 47907, U.S.A.

Received 7 April 1998; received in final form 17 July 1998

Abstract

Photographic studies of near-saturated pool boiling at various surface orientations were conducted in order to determine the critical heat flux (CHF) trigger mechanism associated with each orientation. Based on the vapor behavior observed just prior to CHF, it is shown that surface orientations can be divided into three regions: upward-facing (0–60°), near-vertical (60–165°), and downward-facing (>165°); each region is associated with a unique CHF trigger mechanism. In the upward-facing region, the buoyancy forces remove the vapor vertically off the heater surface. The near-vertical region is characterized by a wavy liquid–vapor interface which sweeps along the heater surface. In the downward-facing region, the vapor repeatedly stratifies on the heater surface, greatly decreasing CHF. The vast differences between the observed vapor behavior within the three regions indicate that a single overall pool boiling CHF model cannot possibly account for all the observed orientation effects, but instead three different models should be developed for the three regions. Upward-facing surfaces have been examined and modeled extensively by many investigators and a few investigators have addressed downward-facing surfaces, so this paper focuses on modeling the near-vertical region. The near-vertical CHF model incorporates classical two-dimensional interfacial instability theory, a separated flow model, an energy balance, and a criterion for separation of the wavy interface from the surface at CHF. The model was tested for different fluids and shows good agreement with CHF data. Additionally, the instability theory incorporated into this model accurately predicts the angle of transition between the near-vertical and downward-facing regions.

Nomenclature

b ratio of wetting front length to vapor wavelength
c wave speed
c_i imaginary component of wave speed
c_p specific heat at constant pressure
c_r real component of wave speed
C_{CHF} pool boiling CHF orientation coefficient used by El-Genk and Guo [1]
d heater diameter
f_i interfacial friction factor
g_e Earth's gravity
h_{fg} latent heat of vaporization
H mean layer thickness
k wave number $[2\pi/\lambda]$
k_c critical wave number $[2\pi/\lambda_c]$
K_{0° dimensionless CHF for horizontal upward-facing orientation
L heater length
P pressure
$\overline{P_f - P_g}$ mean interfacial pressure difference in wetting front
q_l localized heat flux in wetting front
q_m critical heat flux (CHF)
$q_{m,0^\circ}$ critical heat flux (CHF) for the horizontal upward-facing orientation
t time
T temperature
T_{sat} fluid saturation temperature
ΔT_{sub} liquid subcooling

* Corresponding author. Tel.: 001 765 494 5705; fax: 001 765 494 0539; e-mail: mudawar@ecn.purdue.edu
[1] Graduate student.
[2] Professor and Director of the Purdue University Boiling and Two-Phase Flow Laboratory.

0017–9310/98/$ - see front matter
PII: S0017–9310(98)00233–6

$\bar{u}$ mean velocity
w heater width
z spatial coordinate in stream-wise direction
z^* distance from leading edge of heater to center of first wetting front [$z^* = \lambda_c$].

Greek symbols
δ vapor wave amplitude; mean vapor layer thickness
η interfacial displacement
η_0 amplitude of interfacial displacement
λ wavelength of interfacial perturbation
λ_c critical wavelength corresponding to onset of instability
ρ density
ρ'' modified density, $\rho'' = \rho \coth(k_c H)$
θ orientation angle measured from horizontal upward-facing position
σ surface tension
τ_i interfacial shear stress.

Subscripts
f saturated liquid
g saturated vapor.

1. Introduction

In recent years, the effects of surface orientation on pool boiling heat transfer and critical heat flux (CHF) have received increased attention because of the potential benefits pool boiling brings to many applications, including cooling of electronic and power devices, heat treating of metallic parts, and cooling of superconductor coils. Previous studies concerning orientation effects on pool boiling CHF have been primarily quantitative in nature, and only a few investigators have attempted to correlate the orientation effects on CHF or provide physical insight into the problem.

Ishigai et al. [2] and Githinji and Sabersky [3], among the first investigators to explore the effects of orientation on pool boiling CHF, noted that CHF decreases drastically when the heated surface is oriented in the horizontal, downward-facing position (180°) because the vapor accumulates and prevents liquid access to the heated surface. Additionally, Ishigai et al. found that CHF decreased with increasing heater area when the heater to the surrounding insulation surface area ratio was held constant. Similar trends were reported by Anderson and Bova [4]. Numerous other pool boiling CHF studies examined orientation effects, and in general these investigations found that CHF decreases as orientation changes from upward-facing horizontal (0°) to vertical (90°) to downward-facing horizontal (180°). Previous experimental studies concerning orientation effects on pool boiling CHF are given in Table 1 along with a summary of the relevant experimental conditions. For consistency, the angle of inclination is referenced from the horizontal upward-facing orientation (0°), even if a particular study utilized a different frame of reference.

Vishnev [28] was the first to correlate the effects of orientation on pool boiling CHF, and his correlation is still the most widely utilized. El-Genk and Guo [1] and Chang and You [21] also developed CHF orientation correlations, and recently, Brusstar and Merte [20, 29] developed an empirical CHF model for pool and flow boiling. El-Genk and Guo avoided the use of a single universal correlation for all fluids; instead, they derived separate correlations for three fluids based on data from the literature. Table 2 summarizes the different correlations and models that incorporate orientation effects on pool boiling CHF. Models and correlations that have been developed strictly for vertical surfaces, such as those by Lienhard and Dhir [30] and Mudawar et al. [26], are not included in Table 2 since they were not intended for angles other than 90°.

Figure 1 compares existing orientation CHF data with the correlations by Vishnev [28], El-Genk and Guo [1] and Chang and You [21], and the empirical model by Brusstar and Merte [20, 29] for (a) cryogenic and (b) non-cryogenic fluids. Since the present investigation only addresses near-saturated conditions, studies where the subcooling was greater than 5° were not included in Fig. 1. Data points that were not tabulated in the literature were obtained from the published plots by scanning in the plot and then digitizing the plot axes and the data of interest. All of the data were normalized with upward-facing horizontal CHF values that were obtained from the same study as the referenced data point. Most investigations that did not include horizontal tests were omitted from the plot, but the data from Guo and El-Genk [17] were included because they are widely referenced; additionally, Guo and El-Genk did recommend a horizontal CHF value for normalizing the data.

Despite the large amount of scatter, Fig. 1 shows the correlation by Vishnev [28], which was originally derived for cryogenic fluids, provides a good fit for cryogenic fluids and a lower bound for non-cryogenic fluids. The correlation by Chang and You [21] provides an upper bound for both the cryogenic and non-cryogenic fluids. For the cryogenic data, Fig. 1(a), it is interesting that although the upward-facing horizontal CHF values differed greatly between investigations (e.g., 0.55 to 1.41 W cm^{-2} for liquid helium and 17.0 to 31.3 W cm^{-2} for liquid nitrogen), orientation data from each investigation collapsed together to reveal similar trends.

The model by Brusstar and Merte [20, 29] has several limitations. The original formulation of the model [20] reduces to the equation given in Table 2 only if the CHF values for the horizontal and vertical orientations are the same, which is a questionable assumption, as Fig. 1

Table 1
Experimental studies concerning effects of orientation on pool boiling CHF

Reference	Fluid	Boiling surface $w \times L$, or d (thickness) (mm)	P (kPa)	Boiling state	Angles of inclination
Ishigui et al. (1961) [2]	Water	Copper 25 and 50 dia. (150)	101.3	Steady; saturated	180°
Githinji and Sabersky (1963) [3]	Isopropyl alcohol	Chromax 3.2×101.6 (0.025)	101.3	Steady; highly subcooled	0°, 90°, 180°
Lyon (1965) [5]	Liquid helium	Platinum 9.91 dia. (8.0)	6.0–228.0	Steady; saturated	0°, 45°, 67.5°, 90°, 112.5°, 135°, 157.5°, 180°
Katto et al. (1970) [6]	Water	Copper 10 dia.	3.0–46.5	Steady; saturated	0°, 90°
Anderson and Bova (1971) [4]	Freon 11	Metal plate heated by circulating hot water 50.8, 152.4, and 304.8 dia.	101.3	Steady; saturated	180°
Jergel and Stevenson (1971) [7], (1972) [8]	Liquid helium	Copper [7]; aluminum [8] 15 dia. (10)	101.3	Steady; saturated	0°, 90°, 180°
Merte et al. (1973) [9]	Liquid hydrogen, liquid nitrogen	Copper 75 dia.	98.6–102.7	Quenched; saturated	0°, 90°, 180°
Bewilogua et al. (1975) [10]	Liquid helium	Copper 12.5 dia.	6.4–210.4	Steady; saturated	0°, 90°, 135°, 165°
Vishnev et al. (1976) [11]	Liquid helium	Stainless steel 96×10.4 (0.063)	101.3	Steady; saturated	0°, 30°, 45°, 60°, 135°, 90°, 120°, 150°, 180°
Deev et al. (1977) [12]	Liquid helium	Copper 30×30	101.3–228.0	Steady; saturated	0°, 90°
Gogonin and Kutateladze (1978) [13]	Ethanol	Stainless steel 5×150 (0.5) 10×150 (0.5) 20×150 (0.5)	101.3–5200.0	Steady; saturated	0°, 180°
Beduz et al. (1988) [14]	Liquid nitrogen	Copper; aluminum 50×50 (6.0)	101.3	Steady; saturated	0°, 90°, 125°, 155°, 165°, 170°, 176°
Nishio and Chandratilleke (1989) [15]	Liquid helium	Copper 20 dia. (30)	101.3	Steady; saturated	0°, 45°, 90°, 135°, 175°, 179°
You (1990) [16]	FC-72	Platinum on glass 5×5 (0.08)	101.3	Steady; subcooled	0°, 90°, 150°, 175°, 180°
Guo and El-Genk (1992) [17]	Water	Copper 50.8 dia. (12.8)	101.3	Quenched; saturated	90°, 135°, 150°, 165°, 170°, 175°, 180°

(*continued on next page*)

Table 1 (*continued*)
Experimental studies concerning effects of orientation on pool boiling CHF

Reference	Fluid	Boiling surface $w \times L$, or d (thickness) (mm)	P (kPa)	Boiling state	Angles of inclination
Gribov et al. (1993) [18]	Water	Stainless steel 10×110 (0.1)	101.3	Steady; saturated	135°, 150°, 165°, 176°
Granovskii et al. (1994) [19]	Water	Stainless steel 200×100 (1.0)	101.3	Steady; saturated	180°
Brusstar and Merte (1994) [20]	R113	Copper 19.1×38.1 Low velocity flow boiling (0.04 m s^{-1})	Pressure set to provide desired subcooling ($T_f = 322$ K)	Steady; near-saturated and subcooled	0°, 30°, 90°, 120°, 135°
Chang and You (1996) [21]	FC-72	Copper 10×10 (1.5)	101.3	Steady; saturated	0°, 45°, 90°, 135°, 180°
Reed (1996) [22]	FC-87	Copper 12.7×12.7 (6.3)	101.3	Steady; near-saturated	0°, 15°, 30°, 45°, 60°, 75°, 90°, 105°, 120°, 135°, 150°, 165°, 180°
Reed and Mudawar (1997) [23]	FC-87, FC-72	Copper 12.7×12.7 (6.3)	101.3	Steady; near-saturated	0°, 45°, 90°, 135°, 180°
Chu et al. (1997) [24]	Water	Aluminum 610 dia. (100)	101.3	Quenched; saturated	180°
Yang et al. (1997) [25]	Water	Stainless steel 20×200 (0.5) 25×200 (0.5) 30×150 (0.5) 40×150 (0.5)	101.3	Steady; saturated	0°, 30°, 90°, 120°, 130°, 150°, 174°, 176°, 178°, 180°
Mudawar et al. (1997) [26]	Water FC-72	Copper 12×62 (6.3) 12.7×12.7 (6.3) 10×10 (6.3) 10×30 (6.3) 10×110 (6.3)	101.3	Steady; near-saturated	0°, 15°, 30°, 45°, 60°, 75°, 90°
Brusstar et al. (1997) [27]	R113	Copper 19.1×38.1 Low velocity flow boiling (0.04 m s^{-1})	Pressure set to provide desired subcooling ($T_f = 322$ K)	Steady; subcooled	0°, 30°, 60°, 90°, 120°, 135°, 150°, 165°, 175°
Present study	FC-72 PF-5052	Copper 12.7×12.7 (6.3) 3.2×35.0 (7.6)	101.3	Steady; near-saturated	0°, 30°, 45°, 60°, 75°, 90°, 120°, 135°, 150°, 165°, 170°, 175°, 180°

illustrates. Additionally, the original formulation of the model [20] balances buoyancy and drag forces, whereas the recent formulation of the model [29] characterizes the drag force as negligible. The revised derivation [29] is based on an experimentally observed relationship between bubble residence time and CHF values from Brusstar et al. [27], and not on any physical mechanism that would result in CHF. Furthermore, while this exper-

Table 2
Correlations and empirical models describing effects of orientation on pool boiling CHF

Reference	Correlation or model[a]	Validity and other comments
Vishnev (1974) [28]	$\frac{q_m}{q_{m,0^\circ}} = \frac{(190-\theta)^{0.5}}{190^{0.5}}$	• Correlation based on fit of liquid helium data from Lyon [5] and Jergel and Stevenson [7, 8]. • $q_{m,0^\circ}$ is the CHF value for the heater oriented in the horizontal upward-facing position ($\theta = 0^\circ$).
El-Genk and Guo (1993) [1]	$q_m = C_{CHF,f}(\theta)\rho_g h_{fg}\left[\frac{\sigma(\rho_f-\rho_g)g_e}{\rho_g^2}\right]^{1/4}$ where $C_{CHF,water}(\theta) = 0.034+0.0037\,(180-\theta)^{0.656}$ $C_{CHF,liq.nitrogen}(\theta) = 0.033+0.0096(180-\theta)^{0.479}$ $C_{CHF,liq.helium}(\theta) = 0.002+0.0051(180-\theta)^{0.633}$	• Water correlation based on fit of data from Guo and El-Genk [17]. • Liquid nitrogen correlation based on fit of data from Beduz et al. [14]. • Liquid helium correlation based on fit of data from Vishnev et al. [11]. • Data from Lyon [5] and Nishio and Chandratilleke [15] were not included when creating the correlation because values for $q_{m,0^\circ}$ were much higher than those of Vishnev et al. [11].
Chang and You (1996) [21]	$\frac{q_m}{q_{m,0^\circ}} = 1.0-0.000120\,\theta\tan(0.414\,\theta)$ $-0.122\sin(0.318\,\theta)$	• Correlation based on fit of FC-72 data from authors. • Checked against CHF data obtained with nitrogen [14], water [17], liquid helium [11] and subcooled FC-72 [16]. Most data fell between Vishnev's correlation [28] (lower bound) and authors' correlation (upper bound).
Brusstar and Merte (1997) [29]	$\frac{q_m}{q_{m,0^\circ}} = \begin{cases} 1.0 & 0^\circ < \theta \leqslant 90^\circ \\ (\sin\theta)^{1/2} & 90^\circ \leqslant \theta < 180^\circ \end{cases}$	• Model is a reduced form applicable only to pool boiling. Full model predicts CHF for flow boiling as well. • Empirical model based on an experimentally observed relationship between bubble residence time and CHF value. This relationship was only shown to be valid for $90^\circ \leqslant \theta < 165^\circ$, but was utilized in the model for all angles. • Model assumes that the vapor departing from the surface is spherical in shape. • Model does a fair job predicting R113 CHF values for angles less than 165°, but was not tested for other fluids. • Pool boiling form of model originally derived in [20] utilizing a different set of assumptions. Original model was based on a balance of buoyancy and drag forces, and reduced to the equation shown only if $q_{m,0^\circ} = q_{m,90^\circ}$.

[a] θ is in degrees.

imental relationship was only shown to be valid for $90 \leqslant \theta < 165^\circ$, it was utilized in the model for all angles. Even for the applicable angles, the relationship is somewhat questionable for pool boiling because the experiments were actually low velocity flow boiling tests with a confining channel height of 25.4 mm, which may not be representative of actual pool boiling conditions. A second weakness in the Brusstar and Merte model as

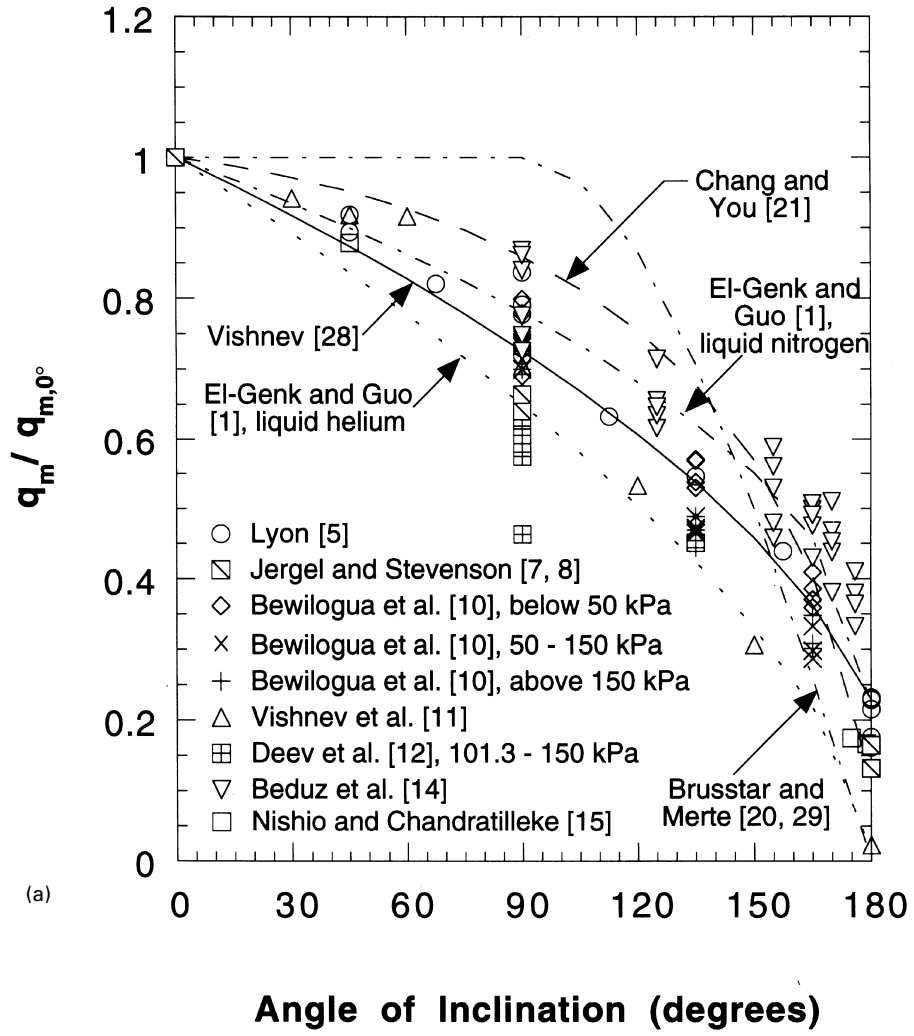

Fig. 1. Effects of orientation on CHF for (a) cryogenic fluids and (b) non-cryogenic fluids.

derived in [29] is the assumption that the vapor departs from the surface in spherical bubbles. This is contrary to observed vapor behavior, especially at inclinations of 90° or greater where the vapor rarely departs from the surface but instead slides along the heater surface. Mudawar et al. [26] showed that at high heat fluxes near CHF, vapor on vertical surfaces forms a Helmholtz wave which sweeps along the heater surface. Even the vertical photographs by Brusstar et al. [27] show the vapor traversing the surface rather than departing from the surface in spherical bubbles. Additionally, for large inclinations close to 180°, Beduz et al. [14], Yang et al. [25], and Chang and You [21] noted that near CHF the vapor sliding along the heater surface stretches and merges with other vapor bubbles until the vapor shape is greatly elongated; this elongated vapor mass continues to move along the surface until the vapor mass passes off the edge of the surface. Although the Brusstar and Merte model did a fair job of predicting R-113 data obtained by Brusstar and Merte [20] and Brusstar et al. [27], Fig. 1(b) shows that the model is a poor representation of the bulk of the normalized CHF pool boiling orientation data.

The above literature review reveals the need for additional analysis regarding orientation effects on pool boiling CHF. Key objectives of this study are: (a) to explore the CHF trigger mechanism for different orientations and (b) to develop a theoretically-based CHF model capable of predicting the orientation effects. To accomplish these objectives, extensive photographic studies of near saturated pool boiling were conducted at different orientations to determine the physical mechanisms that trigger CHF.

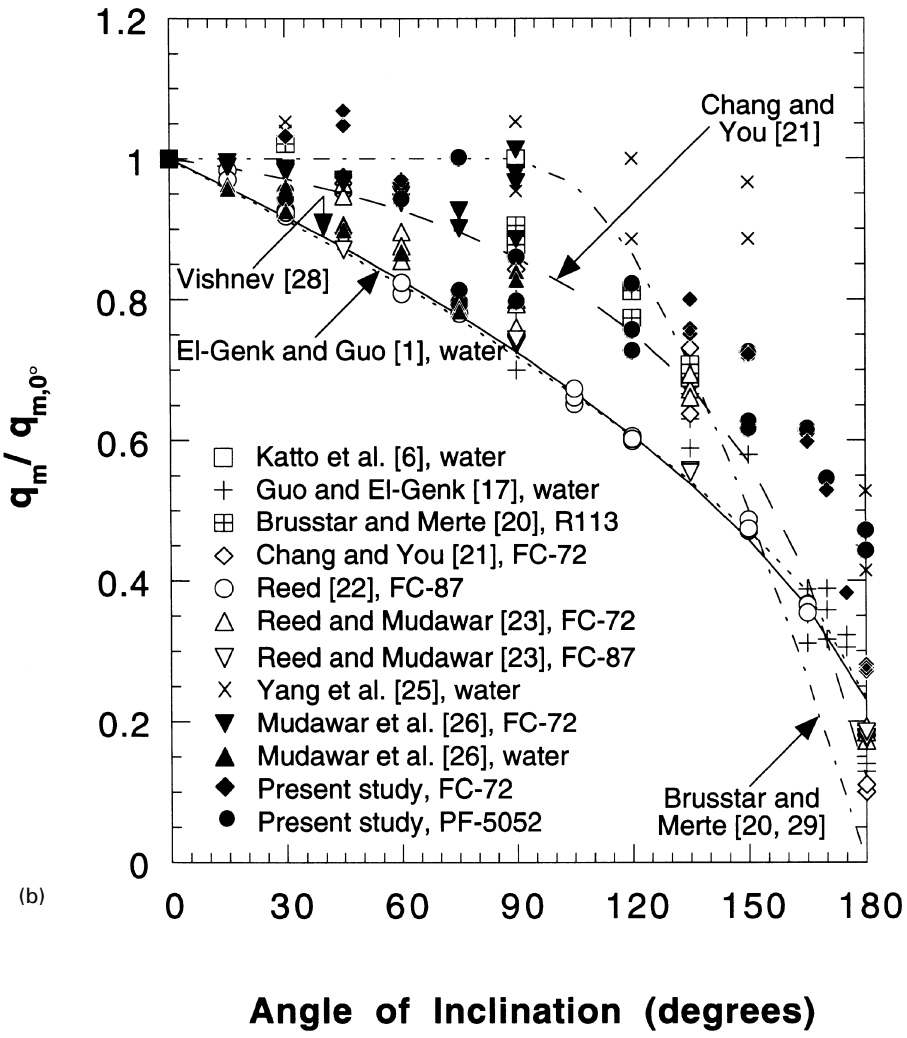

Fig. 1 (*continued*)

2. Experimental methods

Two different heater configurations, both shown in Fig. 2(a), were used in this study. The first configuration was a 12.7×12.7 mm^2 copper block heated by a thick-film resistor silver soldered to the underside of the copper block. The second heater configuration was designed to allow a thin slice of the heater surface to be visualized, making the boiling features more discernible and virtually eliminating three-dimensional effects. Constructed from copper, the wetted surface measured 3.2×35.0 mm^2 and was heated by two thick-film resistors that were silver soldered on the wide base and wired in series. Both heaters were imbedded in an insulative G-7 fiberglass plastic substrate to minimize the heat losses through the heaters' sides and back. Hereafter, the first heater configuration will be referred to as the square heater and the second configuration as the thin heater. The square heater tests were conducted with 3M's Fluorinert FC-72, while the thin heater tests were run with 3M's Fluorinert PF-5052. The latter fluid was used because its thermophysical properties are very similar to those of FC-72, and because FC-72 was becoming exceedingly difficult to obtain during the course of the present study. Table 3 compares the thermophysical properties of these two fluids along with those for water and liquid helium.

A computer-based data acquisition system was utilized to take thermocouple and transducer measurements. Thermocouple and transducer readings were sampled 20 times over a time period of 30 s, and a 'measurement' was the average of the 20 readings. Data were recorded at steady-state conditions, defined as those attained when

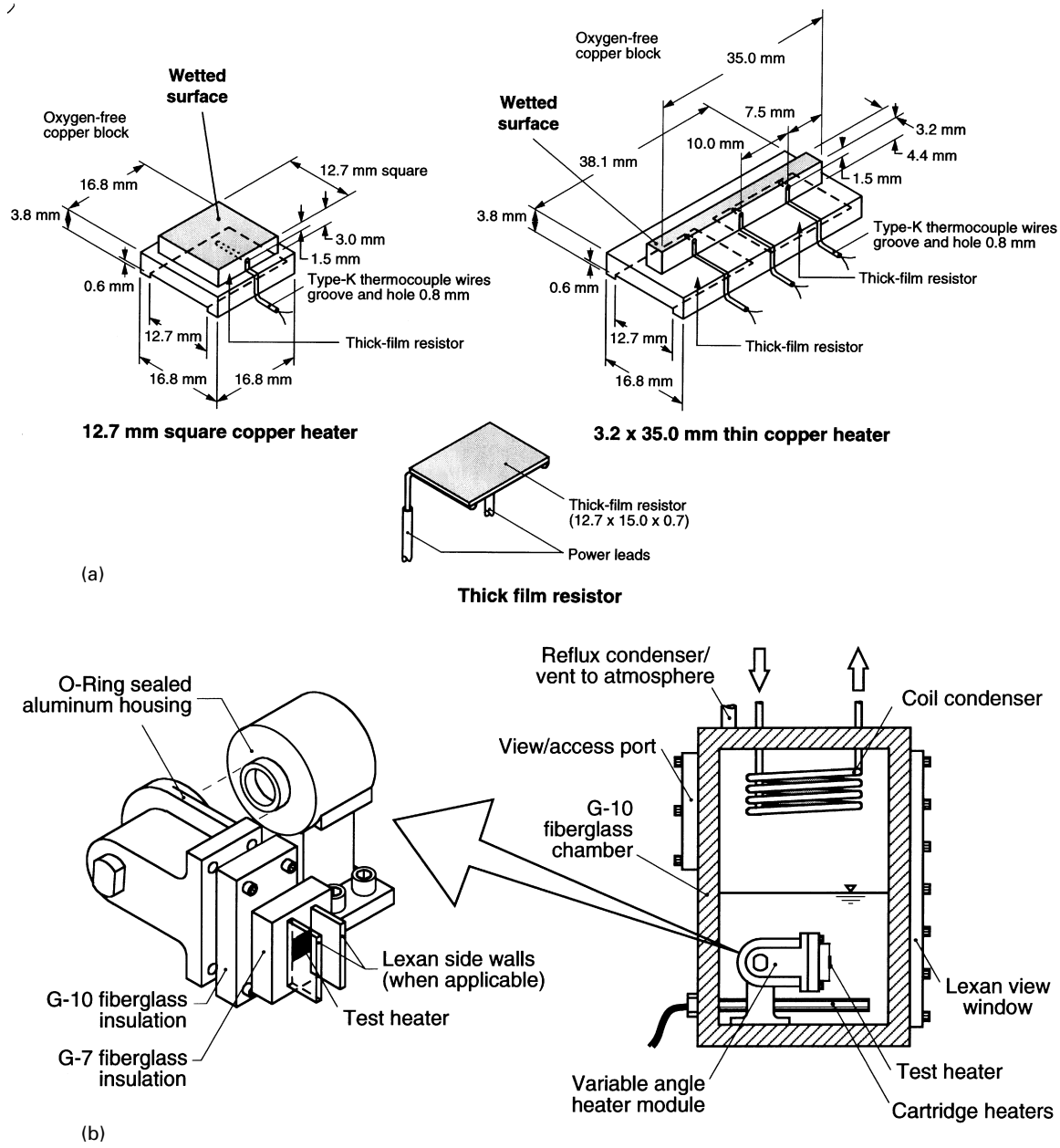

Fig. 2. (a) Test heaters and thick film resistor; (b) pool boiling test facility.

Table 3
Saturated thermophysical properties of different fluids at 1 atm

Fluid	T_{sat} (°C)	ρ_f (kg m^{-3})	$c_{p,f}$ (J kg^{-1} K^{-1})	ρ_g (kg m^{-3})	h_{fg} (kJ kg^{-1})	$\sigma \times 10^3$ (N m^{-1})
FC-72	56.6	1600.1	1102.0	13.43	94.8	8.35
PF-5052	50.0	1643.2	936.3	11.98	104.7	13.0
Water	100.0	957.9	4217.0	0.60	2256.7	58.91
Liquid helium	−268.9	124.9	4545.0	16.89	20.7	0.09

the heater thermocouple had a standard deviation of less than 0.1°C over the 30 s sampling period. Current and voltage transducers were utilized to obtain the heat flux (electrical power input divided by wetted area), and thermocouples placed just beneath the heater surface were used to infer the surface temperature assuming one-dimensional heat conduction between the thermocouple and surface. Only one thermocouple was imbedded in the square heater whereas three thermocouples were imbedded in the thin heater. Since the three surface temperatures of the thin heater differed by less than 0.3°C, the three temperatures were averaged to produce a single mean surface temperature.

Each heater was mounted on an angular rotation platform shown in Fig. 2(b) to facilitate testing at different surface orientations. Figure 2(b) also shows optical-grade Lexan walls which were placed along the sides of the heater surface allowing for a clearer visualization of the liquid-vapor interfacial features. For the square heater, the Lexan walls, which measured 20 mm in height and 39.3 mm in length, were used with tests at orientation angles between 90° and 175°, and some tests at 180°. The boiling curves and CHF values measured during these tests were compared with those from tests by Reed and Mudawar [23] in which no Lexan walls were used; the two were found to produce the same results within the measurement uncertainty of the present experimental apparatus. However, addition of the Lexan walls at orientations less than 90° changed the boiling characteristics and CHF slightly, hence the Lexan walls were not used in these tests. For the thin heater, a single Lexan window 20 mm in height and 39.3 mm in length was attached to the front side of the heater to aid in constraining the transverse movement of the liquid-vapor interface.

Figure 2(b) also shows a schematic of the pool boiling test chamber which was constructed of G-10 fiberglass plastic and fitted on the front and back with Lexan windows. A condenser coil inside the chamber recovered almost all of the vaporized liquid, and an external reflux condenser connected to the chamber's vent acted as a final barrier to any escaping vapor during both deaeration and testing. Three cartridge heaters were used to deaerate fluid prior to testing and to maintain the bulk liquid at near-saturated conditions during testing. To prevent the boiling on the cartridge heaters from influencing CHF, the cartridge heaters were placed near the back of the test chamber and isolated from test heater by a baffle plate (not shown).

Both video images and still photographs were utilized to record the boiling phenomena at various intervals in the nucleate boiling regime as well as just prior to and immediately following CHF. The video images captured a temporal record of the boiling, while the still photographs produced higher resolution images necessary to distinguish and measure different interfacial features. Video images were recorded with a Canon L1 8 mm video camera with a wide angle macro recorder zoom lens, a $2\times$ teleconverter attachment, and extension rings. Still photographs were taken with a Nikon FM2 35 mm camera with a 200 mm lens and assorted attachments. For both the video images and the still photographs, the shutter speed was set at 1/1000. The test apparatus was back-lit with a 2400 W high intensity light source. To minimize the heat added to the test facility from the light source, the light was turned on with the video camera (or just prior to a still shot), and then was turned back off after a few seconds of data recording. To facilitate backlighting, the angular rotation platform was mounted on the bottom of the test facility for orientations less than 150°, as shown in Fig. 2(b), while for orientations equal to or greater than 150° the angular rotation platform was mounted on the side of the test facility.

2.1. Test procedure and measurement uncertainty

The heater surface was lightly polished with Crocus cloth and cleaned with acetone before every test to provide a reproducible surface. The bulk fluid was deaerated by running the test heater and the immersion heaters at saturated boiling conditions for at least 30 min prior to taking data. Although the focus of this study is CHF, data were also obtained in the nucleate boiling regime prior to reaching CHF.

CHF was achieved when a large and rapid rise in surface temperature was detected. CHF was denoted as the highest average heat flux that gave a stable temperature reading plus one half of the last average power increment (~ 0.4 W cm^{-2}). Stable heat fluxes approximately equal to 95% of CHF are hereafter designated as CHF$-$, and heat fluxes slightly greater than CHF, but less than a few seconds after the temperature excursion commenced, are designated as CHF$+$. In order to protect the thick-film resistors from burnout, the data acquisition system was configured with relays to shut off all electrical power to the resistors once CHF caused the heater surface temperature to rise above 110°C, so steady-state film boiling data was not obtained. CHF data for all surface inclinations were repeatable to within $\pm 7\%$.

Propagation of error [31] was utilized in calculating the uncertainties associated with the experimental readings. The thermocouples were calibrated for a maximum uncertainty of ± 0.1°C. At heat fluxes close to CHF, the uncertainty in the heat flux due to instrumentation limitations was estimated to be 5.5%, while the heat losses through the G-7 insulation were estimated to be less than 5% for the square heater and close to 12% for the thin heater. Because the heat losses from the thin heater were so much greater than from the square heater, the thin heater tests were utilized primarily to capture video images and still photographs so that the liquid–vapor interfacial features were clearly discernible.

3. Experimental results

Since a single image of the boiling process can easily be misinterpreted, the present authors captured extensive video segments of the near-wall interfacial features at different surface inclinations and examined them frame by frame to determine which boiling characteristics appeared repeatedly at each orientation. Only the still photographs that were most representative of the boiling process are presented in this paper.

Near CHF, vapor on both the square and thin heaters exhibited the same general trends for any given orientation. While boiling from the square surface is more representative of a real heater, the thin heater configuration allows the interfacial features to be more clearly ascertained. Figure 3 shows CHF− on the thin heater for surfaces at 0, 30, 60, 90, 120, 150, and 180°. At heat fluxes near CHF the boiling process can be divided into three regions with categorically different vapor behavior. The first is the *upward-facing region* which includes 0 and 30°. Here the vapor is removed vertically off the surface by buoyancy. The second is the *near-*

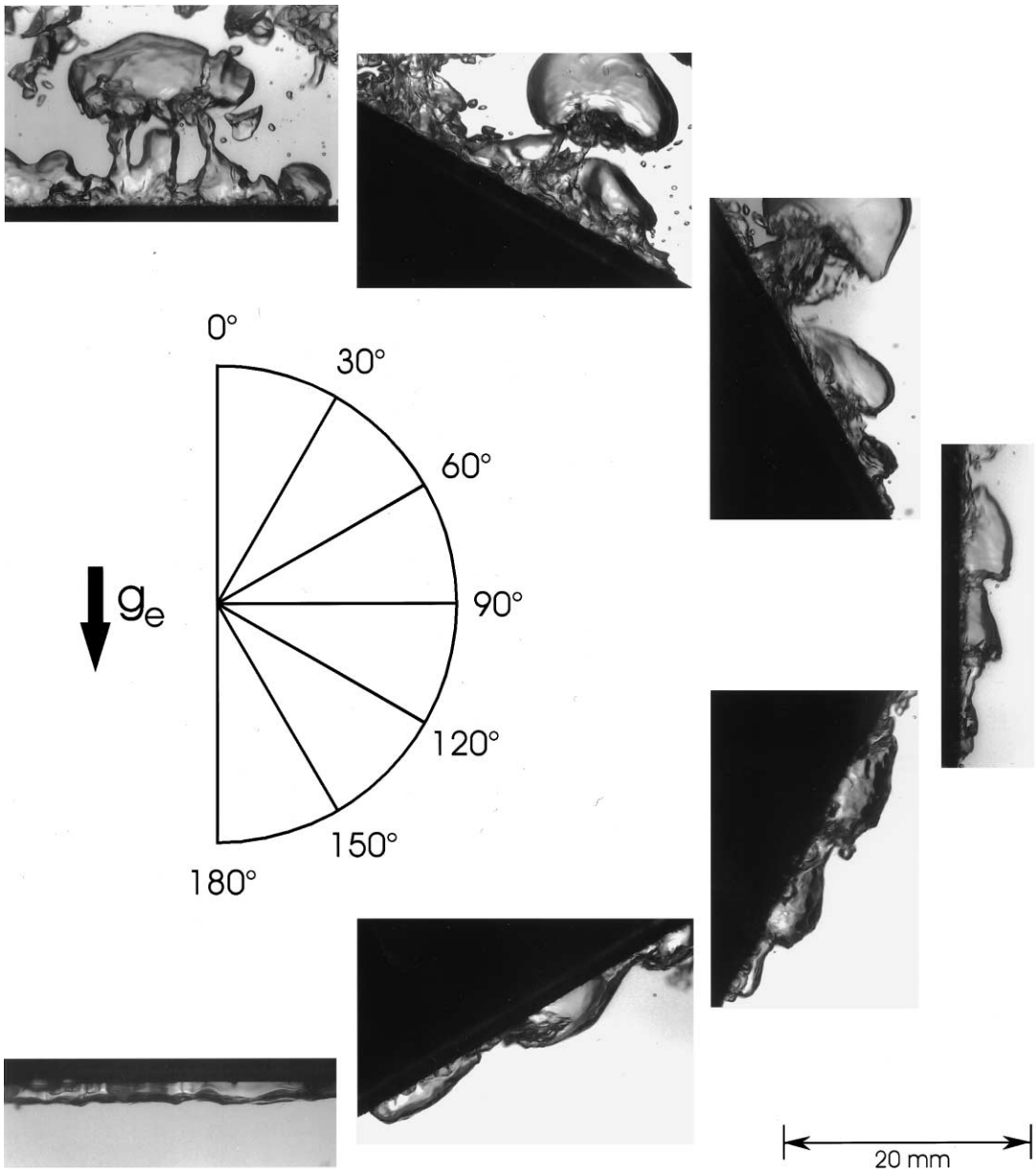

Fig. 3. Thin heater pool boiling photographs at CHF− for various surface orientations.

vertical region, including 90, 120, and 150°, where the vapor travels along the surface and instabilities cause the liquid-vapor interface to be wavy. Finally, at orientations near 180°, stratification of the vapor along the heated surface occurs. This third region is the *downward-facing region*.

In the upward-facing region, represented in Fig. 3 by the 0 and 30° photographs, there is evidence both of large vapor jets, as suggested in the models by Zuber et al. [32] and Lienhard and Dhir [30], as well as significant boiling activity within a thin surface liquid layer, as postulated by Haramura and Katto [33]. However, the present authors urge caution when interpreting the upward-facing photographs. The thin layer of boiling liquid that appears along the surface in the photographs could be the result of edge effects where the copper heater mates with the G-7 insulation. Additionally, these edge effects obscure the view of the boiling interface, leaving both the present upward-facing photographs and horizontal photographs published by previous investigators [34–36] open to different interpretations. The purpose of the present paper is not to address these issues, which have been thoroughly explored in many review papers, including those by Lienhard [37], Katto [38], and Bergles [39]. The only significance of these photographs to the present study is to determine the angular extent of the upward-facing region.

By comparing the photographs taken for surfaces between 30 and 150°, as shown in Fig. 3, it is evident that the vapor behavior changes quite drastically with orientation. At 30° the vapor lifts vertically off the surface. However, as the orientation of the surface becomes more vertical, the vapor is forced to travel along the surface and the motion of the vapor creates interfacial instabilities resulting in the formation of a fairly continuous wavy vapor layer. At 60° the wavy layer travels primarily along the heater surface, but is occasionally disrupted by a vertical release of the vapor. At 90° the liquid-vapor wavy interface travels exclusively along the surface, and boiling is sustained by liquid entrainment near the lower edge of the heater, as well as in *wetting fronts*, where the liquid-vapor interface makes contact with the surface. Between the wetting fronts, the heater experiences dry-out, as the 90° photograph in Fig. 3 shows. The wavy vapor layer observed at 90° is also evident at 120 and 150°.

Figure 3 reveals that near 180° the vapor behavior is again categorically different from the other two regions. In this downward-facing region, individual bubbles which nucleate on the surface grow and coalesce with other bubbles, eventually covering most or all of the heater surface, and then engulfing the surrounding insulation. As the vapor blanket grows, it inevitably reaches an edge where the vapor is released by buoyancy. Liquid is then able to wet the heater surface, causing revival of bubble nucleation and initiating a new boiling/stratification/release cycle.

Clearly, the transition points between the three regions needed to be more accurately defined, so additional data (not presented in this study) were taken with the square heater for surfaces inclined at 45, 75, 165, and 170°. At 45° the boiling exhibited near-horizontal characteristics, while at 75° the wavy vapor motion resembled that of the near-vertical region. This is to be expected, since the vapor behavior at 60° seemed to fluctuate between the two regions while more often exhibiting near-vertical characteristics. At 165° the boiling was still characterized by a wavy vapor layer some of the time, but at 170° the vapor stratified on the downward-facing surface.

Several previous studies reported findings which are consistent with the present observations. Yang et al. [25] noticed a transition in the boiling behavior from vertical-like to downward-facing between 150° and 174°. Additionally, the relationship between the bubble residence time and CHF on which the Brusstar and Merte [29] model is based was shown by Brusstar et al. [27] to be invalid for orientations of 165° and greater. Combining the observations by Yang et al. and Brusstar et al. with present observations, 165° was deemed to be the transition angle between the near-vertical and downward-facing regions.

Figure 4 summarizes the three boiling regions observed at high heat flux conditions leading to CHF: upward-

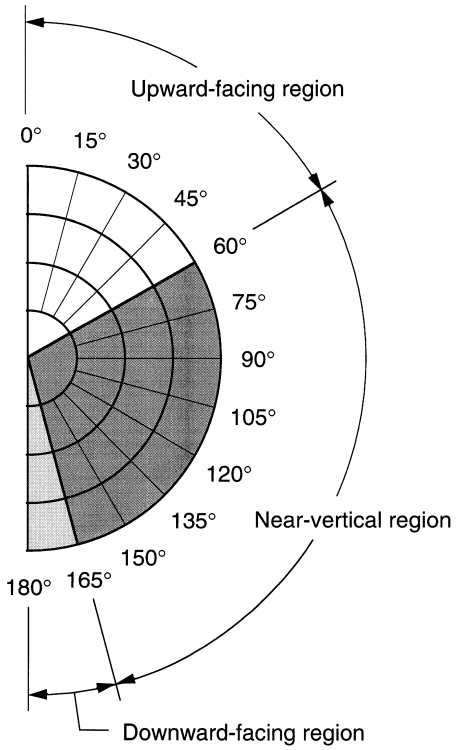

Fig. 4. Pool boiling regions determined from experimental observation of vapor behavior just prior to CHF.

facing region (0 to 60°), near-vertical region (60 to 165°), and downward-facing region (165–180°). Because of the vast differences between the three regions, it can be clearly concluded that three different models should be used to predict pool boiling CHF at the different orientations. Since the horizontal surface, which is very characteristic of the upward-facing region, has been examined and modeled by previous investigators, and a few investigators have addressed downward-facing surfaces, the remainder of this paper will focus on the near-vertical region. This region covers close to 60% of all orientation angles.

4. Vapor behavior in near-vertical region

Figures 5 and 6 depict the changes in vapor behavior on the thin heater with increasing heat flux at 90 and 150°, respectively. These photographic sequences correspond to the near-vertical region. As previously mentioned, great care was exercised to present only the still photographs that are most representative of the boiling process, based on analysis of the multitude of video images.

At very low heat fluxes, Figs 5 and 6 show individual bubbles sliding along the heater surface upon release from nucleation sites. As the heat flux was increased, the individual bubbles coalesced to form larger, oblong vapor bubbles. As the heat fluxes exceeded 50% of CHF, the vapor bubbles became larger and traveled faster, and the vapor began to look more like a wavy layer than a series of long, discrete bubbles.

At heat fluxes close to CHF, the vapor coalesced into a fairly continuous wavy layer. Liquid access to the surface was possible at the lower edge of the heater which sustained vigorous boiling, and at *wetting fronts* where the liquid-vapor interface made contact with the surface. These wetting fronts were approximately one-fourth of the vapor wavelength, and as the wetting front propagated along the heater, the localized surface was cooled intermittently by the boiling in the wetting fronts. Indirect experimental evidence supporting this wetting front description is also available from flow boiling studies by Fiori and Bergles [40] and Hino and Ueda [41, 42] who measured fluctuations in heater surface temperature synchronous with the passage of large vapor masses.

CHF commenced when the liquid–vapor interface of the most upstream wetting front separated from the heater surface, followed by the remaining downstream wetting fronts separating in succession. The CHF+ photograph for 90°, Fig. 5, clearly shows that lift-off has occurred at the wetting fronts. However, at 150°, Fig. 6,

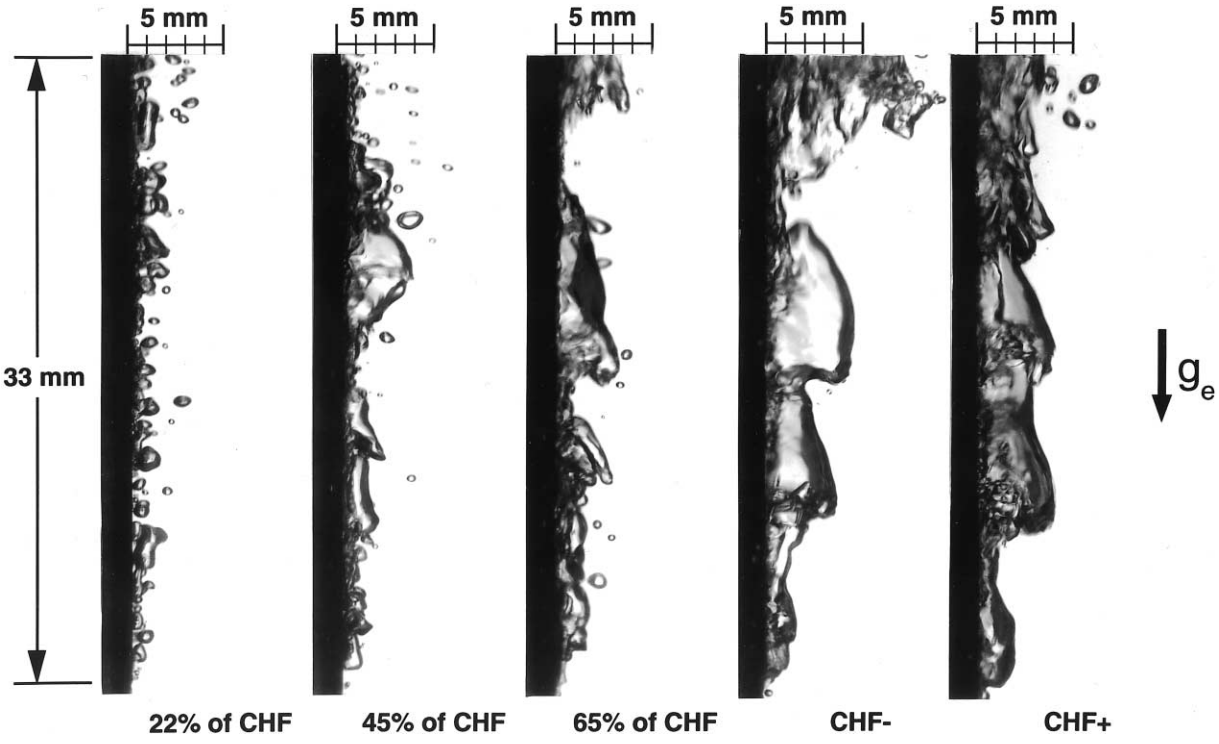

Fig. 5. Pool boiling photographs at increasing heat fluxes for the thin heater oriented at 90°.

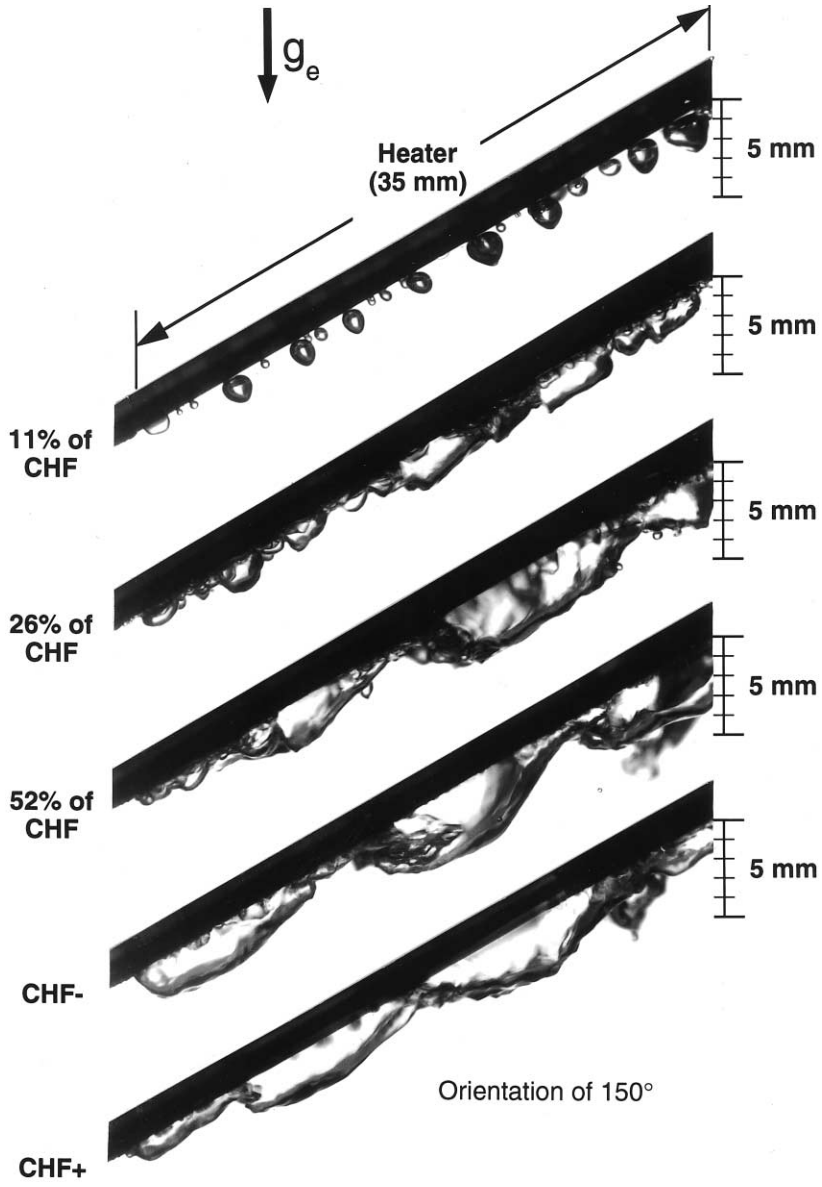

Fig. 6. Pool boiling photographs at increasing heat fluxes for the thin heater oriented at 150°.

the wetting front lifting action was not as prominent as at 90°. Instead, during CHF+, the wetting front was observed to thin out and become virtually non-existent. Despite the different mechanisms, the net result in both cases (90 and 150°) was that the liquid was prevented from contacting the heater surface, inciting CHF.

5. CHF model for near-vertical region

Mudawar et al. [26] performed a photographic study of vertical pool boiling CHF and found that at high heat flux conditions leading to CHF, vertical pool boiling exhibited vapor production patterns similar to those observed in flow boiling experiments by Galloway and Mudawar [43] and Gersey and Mudawar [44]. They also noted that prior to CHF, the curvature of the wetting front created a pressure force which tended to preserve the interfacial contact with the wall. CHF was triggered when this pressure force was overcome by the momentum of the vapor generated at the wetting front, causing the wavy liquid-vapor interface to lift off the heater surface. Based on these observations, they developed a CHF model that incorporated energy balances both at the sur-

face and at the wetting front where lift-off occurred, a two-phase separated flow model, and the Helmholtz instability theory. The present investigation extends the model by Mudawar et al. to include orientation effects in the near-vertical region (60–165°).

5.1. Interfacial instability of vapor layer

Figure 7, adapted from Mudawar et al. [26], shows a schematic of the wavy vapor layer at CHF−. The interfacial waviness can be idealized as a classical two-dimensional hydrodynamic instability. Thus, the wetting fronts are formed when a disturbance in the liquid–vapor interface becomes unstable, growing in amplitude until the interface makes contact with the heater surface. The instability is created primarily by the difference between the vapor and liquid velocities. Close to the leading edge, where the velocity difference is small and thus the wavelength required for instability is large, the interface is stable. However, at a distance equal to the critical wavelength, λ_c, the interface becomes unstable and touchdown first occurs at the stream-wise location $z = z^*$. Although the wetting front propagates along the heater surface at a speed equal to the real component of the wave speed, c_r, the momentum created by the residual liquid left at $z = z^*$ prevents the next disturbance from forming. Therefore, wetting skips every other cycle and wetting fronts are separated by $2\lambda_c$ wavelengths. These same trends were also exhibited in flow boiling studies [44–46]. Additionally, just as in flow boiling, the present photographic study found that the mean value of the wetting front span is equal to one-fourth the separation distance between wetting fronts for all near-vertical orientations. The wave placement shown in Fig. 7 is for a time when the wetting front is first forming, such as $t = 0$ or $t = 2\lambda_c/c_r$. Recent photographic studies by Sturgis and Mudawar [47, 48] have revealed that the upstream wetting front skipping process is completely suppressed in flow boiling at high liquid velocities (> 1 m s^{-1}), and that the wetting front span is slightly smaller than one-fourth of the vapor wavelength at high liquid velocities. However, these new findings do not impact the pool boiling conditions of the present study.

In order to determine the critical wavelength, λ_c, classical instability theory [49, 50] is employed. Assuming inviscid, irrotational, incompressible, two-dimensional flow, the interfacial pressure difference resulting from a sinusoidal disturbance of the form $\eta(z,t) = \eta_0 e^{ik(z-ct)}$

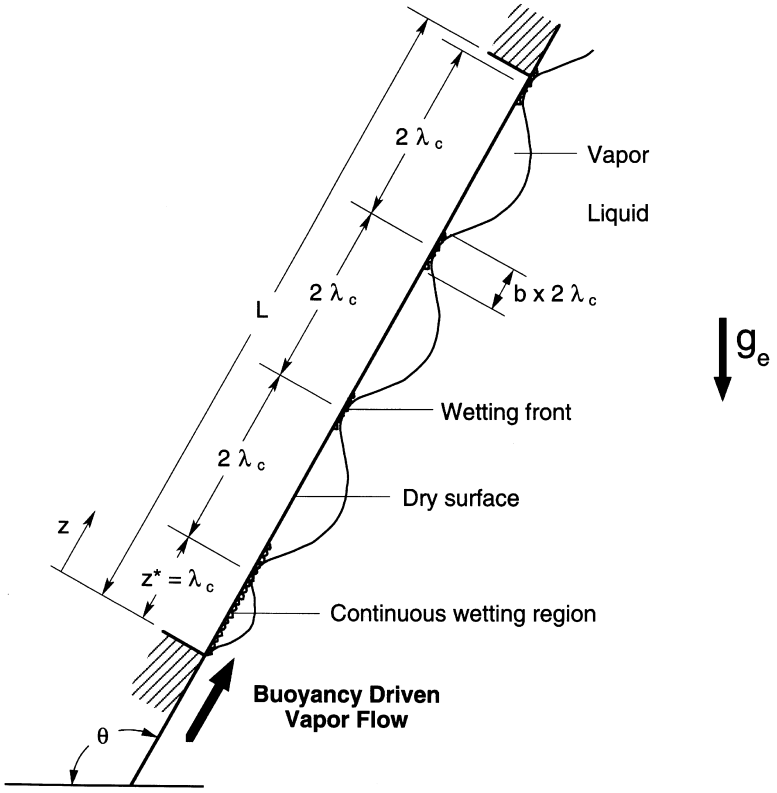

Fig. 7. Wetting front propagation along a near-vertical surface, shown at $t = 2\lambda_c/c_r$.

perpendicular to an unperturbed interface can be expressed as:

$$P_f - P_g = -\eta k\left[\rho_f \frac{\cosh[k(H_f-\eta)]}{\sinh[k(H_f)]}(c-\bar{u}_f)^2 + \rho_g \frac{\cosh[k(H_g+\eta)]}{\sinh[k(H_g)]}(\bar{u}_g-c)^2\right] - \eta(\rho_f-\rho_g)g_e\cos\theta = -\sigma k^2\eta \quad (1)$$

where $g_e \cos\theta$ is the body force per unit mass perpendicular to the unperturbed interface and H_f and H_g are the mean liquid and vapor layer thicknesses, respectively. Since the liquid and vapor wave speeds are constant at any point along the interface, the wave speed can easily be found from equation (1) at the axial location where the sinusoidal disturbance, η, is equal to zero, such that:

$$c = \frac{\rho_f''\bar{u}_f + \rho_g''\bar{u}_g}{(\rho_f''+\rho_g'')} \pm \sqrt{\frac{\sigma_k}{(\rho_f''+\rho_g'')} - \frac{\rho_f''\rho_g''(\bar{u}_g-\bar{u}_f)^2}{(\rho_f''+\rho_g'')^2} - \frac{(\rho_f-\rho_g)g_e\cos\theta}{k(\rho_f''+\rho_g'')}} \quad (2)$$

where $\rho_g'' = \rho_g \coth(k_c H_g)$ and $\rho_f'' = \rho_f \coth(k_c H_f)$. For pool boiling, $\bar{u}_f = 0$, $\rho_f'' = \rho_f$, and H_g is equal to the wave amplitude, δ, also denoted as the mean vapor thickness. Additionally, the mean vapor velocity, $\bar{u}_g$, and the mean vapor thickness, δ, can be calculated for any stream-wise location and heat flux using the separated flow model described in Appendix A.

When the liquid–vapor interface becomes unstable, the term under the radical in equation (2) becomes negative, and c must be expressed as an imaginary number, where $c = c_r + ic_i$. The liquid–vapor velocity difference always produces a destabilizing effect and the surface tension a stabilizing effect. The density gradient is traditionally considered destabilizing; however, for orientations greater than 90° the vapor resides above the liquid, producing a stabilizing effect as $\cos\theta$ becomes negative. Using the experimental CHF values obtained in the present study for FC-72 to calculate $\bar{u}_g$ and δ from the separated flow model described in Appendix A, the term under the radical in equation (2) was computed and plotted in Fig. 8a versus wavelength for different orientations. Clearly, at orientations of 165° or greater, the liquid-vapor interface is *always* stable. Although not shown in Fig. 8a, the largest orientation that produces unstable waves was found to be 161°. Interestingly, 165° is the orientation where, based on experimental observations of the vapor behavior just prior to CHF, departure from the near-vertical region to the downward-facing region began to take effect. The boiling at 165° was sometimes but not always characterized by the wavy liquid–vapor interface attributed to the near-vertical region, and so it is truly a *transition* orientation.

For orientations where instability does exist, the critical wave number, or the wave number that produces a neutrally stable wave, can be calculated by setting the radical in equation (2) equal to zero. For pool boiling, the critical wave number reduces to

$$k_c = \frac{2\pi}{\lambda_c} = \frac{\rho_f\rho_g''(\bar{u}_g)^2}{2(\rho_f+\rho_g'')\sigma} + \sqrt{\left[\frac{\rho_f\rho_g''(\bar{u}_g)^2}{2(\rho_f+\rho_g'')\sigma}\right]^2 + \frac{(\rho_f-\rho_g)g_e\cos\theta}{\sigma}}. \quad (3)$$

It should be noted that k_c must be obtained iteratively since ρ_g'' is a function of k_c.

Two special cases of the critical wavelength are the Taylor wavelength, which occurs when the liquid–vapor velocity difference, $\bar{u}_g - \bar{u}_f$, goes to zero, and the Helmholtz wavelength, which occurs when the gravitational force, $g_e \cos\theta$, goes to zero. Figure 8b compares the critical wavelength computed using equation (3) with the Taylor and Helmholtz critical wavelengths for near-vertical pool boiling of saturated FC-72. The experimental pool boiling CHF values obtained in the present study for FC-72 were utilized in conjunction with the separated flow model described in Appendix A to obtain the mean vapor velocity, $\bar{u}_g$, and the mean vapor thickness, δ, at an axial location of $z = \lambda_c$. While the Taylor and Helmholtz wavelengths greatly simplify the computation of critical wavelength and thus CHF, Fig. 8b clearly shows that neither wavelength provides an acceptable approximation to justify its use. Additionally, contrary to the general wavelength predictions, the Taylor wavelength predicts stable waves for orientations greater than 90°, and the Helmholtz wavelength predicts unstable waves regardless of orientation. However, by retaining the general form of the critical wavelength, equation (3), the transition angle between the near-vertical and downward-facing regions is accurately predicted, since the largest orientation that produces unstable waves is 161°.

5.2. Surface energy balance at CHF and CHF trigger mechanism

A surface energy balance detailed by Galloway and Mudawar [45] yields the following expression for CHF:

$$q_m = bq_l\left[1 - \frac{b\lambda_c}{4(L-z^*)}\right] \quad (4)$$

where the coefficient in the brackets accounts for continuous wetting in the region $0 < z < z^*$ and any partial wetting fronts in the downstream region, and is close to unity for all operating conditions experienced in the present investigation. A photographic study of flow boiling by Galloway and Mudawar [43, 45] revealed that the length of each wetting front was one-fourth the separation distance between wetting fronts. Photographs from the present investigation showed that all orientations in the near-vertical region exhibited the same

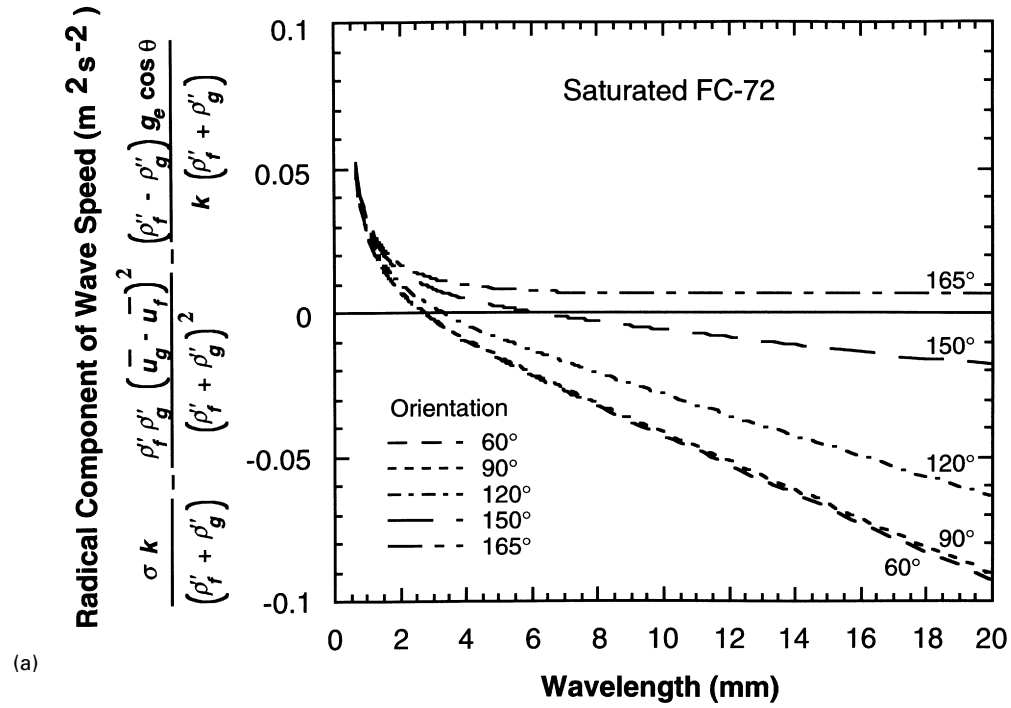

(a)

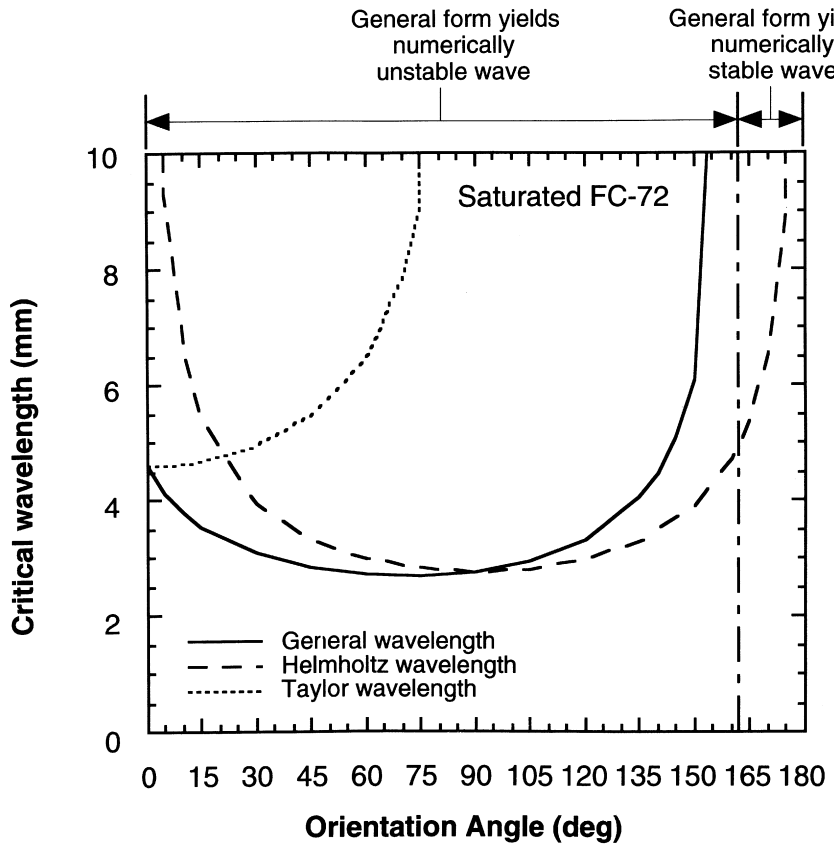

(b)

Fig. 8. Instability theory applied to the near-vertical CHF model: (a) radical component of wave speed for various surface orientations and (b) comparison of general critical wavelength with Taylor and Helmholtz critical wavelengths.

trend; i.e., CHF is about one-fourth the heat flux concentrated in the wetting fronts.

As previously discussed, the photographic study revealed that CHF is initiated when the liquid–vapor interface of the most upstream wetting front separates from the heater surface. The interfacial curvature of any wetting front can be described as a sinusoidal shape with a wavelength of $2\lambda_c$, or $\eta(z,t) = \delta \cos[k(z-c_r t)]$, where $k = 2\pi/(2\lambda_c)$. Prior to CHF, the interfacial curvature produces a pressure force on the interface which tends to maintain liquid contact with the heater surface in the trough regions of the waves. However, at CHF, the localized heat flux in the wetting front, q_l, is large enough that the normal momentum of vapor generated in the wetting front just exceeds the pressure force exerted upon the interface. Therefore, at CHF

$$\rho_g\left[\frac{q_l}{\rho_g h_{fg}\left(\frac{c_{p,f}\Delta T_{sub}}{h_{fg}}\right)}\right]^2 = \overline{P_f - P_g} \tag{5}$$

where the average pressure difference across the interface, $\overline{P_f - P_g}$, is calculated by integrating the pressure difference obtained from equation (1) over the span of the most upstream wetting front, such that the mean interfacial force over the wetting front becomes:

$$\overline{P_f - P_g} = \frac{\int_{3\pi/4k}^{5\pi/4k} -\sigma\delta k^2 \cos[k(z-c_r t)]\,\mathrm{d}(z-c_r t)}{\frac{1}{4}(2\lambda_c)} = 2\sqrt{2}\pi\frac{\sigma\delta}{\lambda_c^2}. \tag{6}$$

As lift-off occurs, the interfacial curvature is reduced, accelerating the interfacial lift-off even further.

Combing equations (4), (5) and (6), and substituting one-fourth for the wetting front span (i.e., $b = 0.25$) yields an expression for CHF which is applicable to flow boiling for both straight and curved heaters, as shown by Galloway and Mudawar [45, 51] and Gersey and Mudawar [46], and to pool boiling in the near-vertical region:

$$q_m = \frac{1}{4}\rho_g h_{fg}\left(1-\frac{\lambda_c}{16(L-z^*)}\right)\left(1+\frac{c_{p,f}\Delta T_{sub}}{h_{fg}}\right)\times\left[(2\sqrt{2}\pi)\frac{\sigma\delta}{\rho_g\lambda_c^2}\right]^{1/2}. \tag{7}$$

The critical wavelength, λ_c, is determined from equation (3) and the mean vapor velocity, $\bar{u}_g$, and the vapor wave amplitude, δ, are calculated at the point where the first wetting front is established, $z = z^* = \lambda_c$, according to the separated flow model described in Appendix A. The present model assumes that the character of the wave is preserved downstream of the first wetting front. Thus, the critical wavelength does not vary with axial direction for $z > \lambda_c$.

5.3. Solution procedure

Predicting CHF for a particular heater orientation required an iterative scheme. First, a value for CHF was estimated and the local velocity, $\bar{u}_g$, and mean vapor layer thickness, δ, were each computed as a function of axial location, z, using the separated flow model. Next, the critical wavelength, λ_c, was calculated from equation (3). Since ρ_g'' is a function of k_c, this in itself was an iterative process that was concluded when the difference in the critical wavelengths was less than 0.0001 mm. Finally, CHF was obtained from equation (7). This CHF value was then utilized as an input for the next iteration. The iterative processes were terminated once the difference in CHF values between consecutive iterations was below 0.001 W cm^{-2} for FC-72 and PF-5052, 0.01 W cm^{-2} for water, and 0.00001 W cm^{-2} for liquid helium.

It should be noted that the present model is only valid for near saturated conditions, since it does not account for condensation at the interface. The model applies only to thick heaters with a length longer than the critical wavelength defined in equation (3). Additionally, this model ignores liquid conduction effects and is therefore not valid for liquid metals.

6. Near-vertical region CHF model predictions

Figure 9a compares existing CHF data for FC-72 with the predictions of the near-vertical model described in the previous section. The coefficient from equation (7) that accounts for the upstream continuous wetting zone and any downstream partial wetting front, or $(1-\lambda_c/16(L-z^*))$, is the partial wetting front coefficient. Figure 9a indicates the partial wetting front coefficient is close to unity for a 12.7 mm long heater. The partial wetting front coefficient is even more negligible for longer heaters. Thus, equation (7) can be reduced to

$$q_m = \frac{1}{4}\rho_g h_{fg}\left(1+\frac{c_{p,f}\Delta T_{sub}}{h_{fg}}\right)\left[(2\sqrt{2}\pi)\frac{\sigma\delta}{\rho_g\lambda_c^2}\right]^{1/2}. \tag{8}$$

Figure 9a also reveals that the model is able to predict the observed transition between the near-vertical and downward-facing regions fairly accurately. The observed transition angle was around 165°, while the near-vertical model predicted a transition orientation of 161°. Additionally, the model does a fairly good job of predicting CHF for orientations between 60° and 150°, but for larger angles approaching 165°, the model shows a steeper decline compared to the experimental data. The differences in the vapor characteristics observed between the upward-facing and the near-vertical regimes was

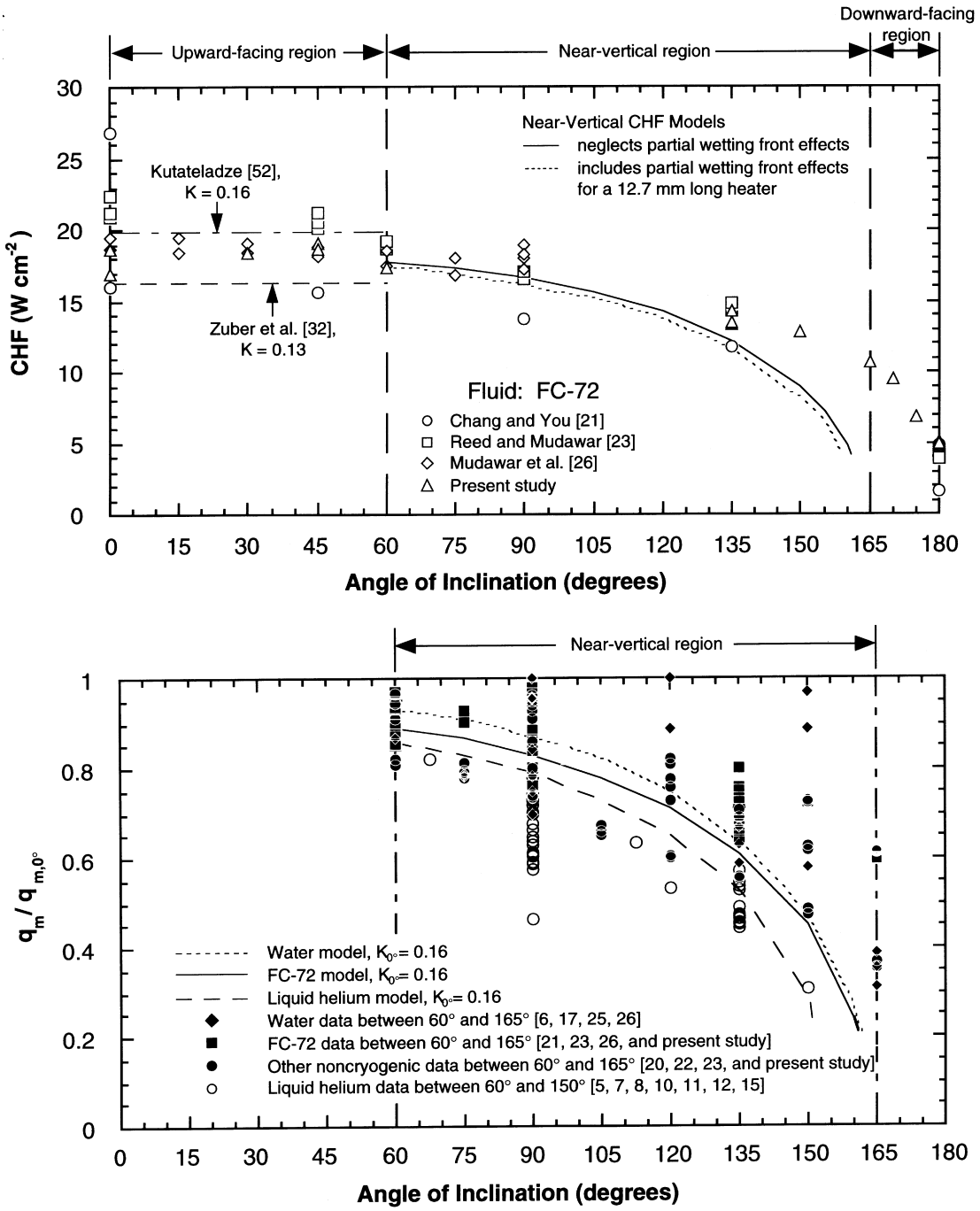

Fig. 9. Comparison of near-vertical CHF model predictions with experimental data for (a) FC-72 and (b) three different fluids with CHF values non-dimensionalized.

more distinct than between the near-vertical and downward-facing regimes. Since the near-vertical model does not address such distinct differences, the transition between the upward-facing and the near-vertical regimes was not predicted analytically.

Figure 9b compares the predictions of the near-vertical model for three fluids, FC-72, water, and liquid helium. The model predictions were non-dimensionalized utilizing the standard CHF expression derived by Kutateladze [52] and Zuber et al. [32],

$$q_{m,0^\circ} = K_{0^\circ}\rho_g h_{fg}\left[\frac{\sigma(\rho_f-\rho_g)g_e}{\rho_g^2}\right]^{1/4} \quad (9)$$

with $K_{0^\circ} = 0.16$ for the horizontal case, as recommended by Kutateladze. The non-dimensionalized form of the model is seen to shift for different fluid properties, supporting El-Genk and Guo's [1] assertion that different correlations be used for different fluids in describing the effects of orientation on CHF. The present model also predicts different transition angles for the different fluids, 150° for liquid helium and 160 to 165° for water and FC-72.

In order to verify the near-vertical model assumption that the interfacial curvature of any wetting front can be described as a sinusoidal shape with a $2\lambda_c$ wavelength, the lengths of the vapor waves were measured from individual frames captured from the videos segments taken at 60, 120 and 150°. The wavelengths were measured from trough to trough, and the stream-wise location of the peak of the wave was taken as the z location of the wave as indicated in Fig. 10. Because of the statistical scatter of the wavelengths, the data were sorted into 1 mm bins and the percent of wavelengths in each bin calculated. For the 60 and 120° orientations, the wavelengths were segregated by stream-wise position into two groups, $\lambda_c < z \leqslant 3\lambda_c$ mm and $3\lambda_c < z \leqslant 6\lambda_c$ mm, but for 150° only one group was utilized since $3\lambda_c$ was very close to the downstream edge of the heater. Additionally, since the continuous wetting zone at the upstream edge of the heater can sometimes appear wave-like, waves at an axial location of $z \leqslant \lambda_c$ were not included in the analysis. The resulting histograms should only be interpreted qualitatively because of the statistically low number of data points.

The histograms in Fig. 10 clearly indicate that at 60° the majority of the wavelengths were close to $2\lambda_c$, which is consistent with the assumptions of the present model and with a similar statistical analysis performed by Mudawar et al. [26] for vertical surfaces ($\theta = 90^\circ$). Additionally, as the waves traveled downstream, a small amount of wave stretching occurred, as indicated by the shift between the $\lambda_c < z \leqslant 3\lambda_c$ and $3\lambda_c < z \leqslant 6\lambda_c$ histograms for the 60° orientation. At 120°, the wavelengths were slightly larger than $2\lambda_c$ upstream ($\lambda_c < z \leqslant 3\lambda_c$), but due to wave stretching and merging the character of the interfacial wave was not preserved as the wave propagated downstream, and the downstream histogram ($3\lambda_c < z \leqslant 6\lambda_c$) did not capture any predominant wavelength. At 150°, there was no dominant wavelength even in the upstream region of the heater. This lack of a predominant wavelength is likely the primary reason why the near-vertical model begins to depart from the data around 150°, even though the wavy liquid–vapor interface is still observed for orientations up to 165°. Nevertheless, the model is still capable of accurately predicting the observed transition angle between the near-vertical and downward-facing regions.

7. Reduction of CHF model for vertical case

For heaters oriented at 90° (vertical case), equation (3), which is used to predict the critical wavelength, reduces to the Helmholtz equation. Furthermore, if shear stress is neglected in the separated flow model, as suggested by Mudawar et al. [53], or if the axial vapor momentum gradient is neglected, as suggested by Mudawar et al. [26], then closed-form expressions can be obtained for the mean vapor velocity, $\bar{u}_g$, and the mean vapor thickness, δ, as shown in Table 4. By combining either of the mean

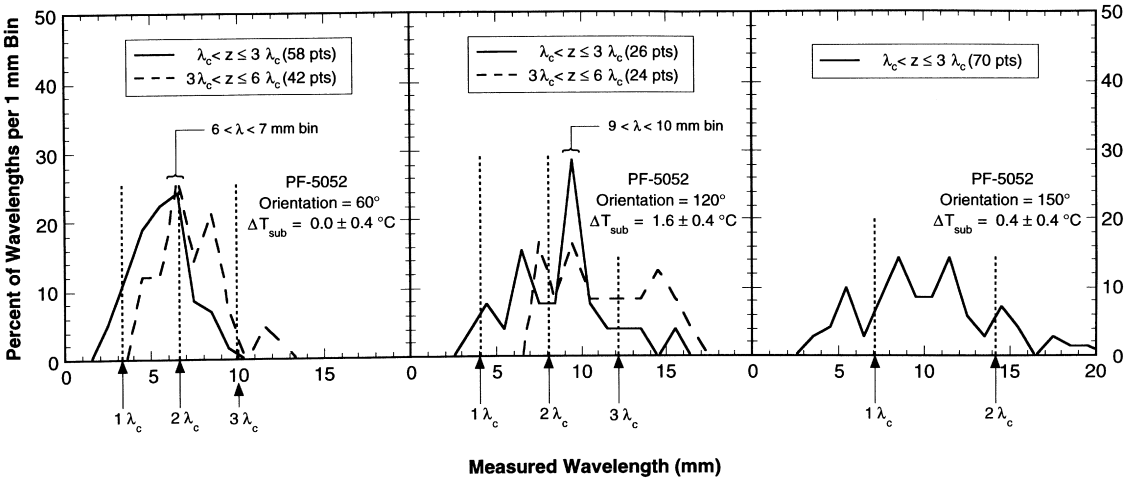

Fig. 10. Histogram of measured wavelengths (plotted at center of each bin and segregated by steam-wise position) for heaters oriented at 60, 120, and 150°.

Table 4
Separated flow and CHF equations for an orientation of 90° neglecting either the shear stress term or the momentum gradient term

	Neglecting shear stress	Neglecting momentum gradient
Vapor velocity	$\bar{u}_g = \left[\frac{2}{3}\left(\frac{\rho_f-\rho_g}{\rho_g}\right)g_e z\right]^{1/2}$	$\bar{u}_g = \left[\left(\frac{\rho_f-\rho_g}{\rho_g}\right)g_e \frac{q_{mz}}{0.5 f_i \rho_g h_{fg}\left[1+\frac{c_{p,f}\Delta T_{sub}}{h_{fg}}\right]}\right]^{1/3}$
Vapor layer thickness	$\delta = \frac{q_m}{\rho_g h_{fg}\left[1+\frac{c_{p,f}\Delta T_{sub}}{h_{fg}}\right]}\left[\frac{2}{3}\left(\frac{\rho_f-\rho_g}{\rho_g}\right)g_e\right]^{-1/2} z^{1/2}$	$\delta = \frac{q_m}{\rho_g h_{fg}\left[1+\frac{c_{p,f}\Delta T_{sub}}{h_{fg}}\right]}\left[\left(\frac{\rho_f-\rho_g}{\rho_g}\right)g_e \frac{q_m}{0.5 f_i \rho_g h_{fg}\left[1+\frac{c_{p,f}\Delta T_{sub}}{h_{fg}}\right]}\right]^{-1/3} z^{2/3}$
Critical wavelength	$\lambda_c = \left[\frac{3\pi\sigma}{(\rho_f-\rho_g)g_e}\frac{\rho_g}{\rho_g''}\left(\frac{\rho_f+\rho_g''}{\rho_f}\right)\right]^{1/2}$	$\lambda_c = \left[2\pi\sigma\left(\frac{\rho_f+\rho_g''}{\rho_f\rho_g''}\right)\right]^{3/5}\left[\left(\frac{\rho_f-\rho_g}{\rho_g}\right)g_e \frac{q_m}{0.5 f_i \rho_g h_{fg}\left[1+\frac{c_{p,f}\Delta T_{sub}}{h_{fg}}\right]}\right]^{-2/5}$
Saturated CHF at pressures much smaller than critical, $\rho_g'' = \rho_g$, δ calculated at $z = 1\ \lambda_c$	$q_m = \frac{1}{8}\left(\frac{\pi}{3}\right)^{1/4}\rho_g h_{fg}\left[\frac{\sigma(\rho_f-\rho_g)g_e}{\rho_g^2}\right]^{1/4}$ [a]	$q_m = 2^{-31/8}\left(\frac{\pi}{f_i}\right)^{1/4}\rho_g h_{fg}\left[\frac{\sigma(\rho_f-\rho_g)g_e}{\rho_g^2}\right]^{1/4}$
Saturated CHF at pressures much smaller than critical, $\rho_g'' = \rho_g$, δ calculated at $z = 1.5\ \lambda_c$	$q_m = 2^{(-7/2)}(3\pi)^{1/4}\rho_g h_{fg}\left[\frac{\sigma(\rho_f-\rho_g)g_e}{\rho_g^2}\right]^{1/4}$	$q_m = 2^{-113/24}3^{5/6}\left(\frac{\pi}{f_i}\right)^{1/4}\rho_g h_{fg}\left[\frac{\sigma(\rho_f-\rho_g)g_e}{\rho_g^2}\right]^{1/4}$ [b]

[a] Solution presented by Mudawar et al. [53]
[b] Solution presented by Mudawar et al. [26]

vapor velocity expressions corresponding to $z = \lambda_c$ with the Helmholtz equation, the critical wavelength can be further reduced to the forms given in Table 4. Mudawar et al. [26, 53] also assumed that $\rho_g'' = \rho_g$. By substituting the equations for critical wavelength and vapor thickness into equation (8), and assuming $\rho_g'' = \rho_g$, the model reduces to a closed form expression for CHF. While the present model calculates the mean vapor thickness, δ, at an axial location of $z = \lambda_c$, the location where the first wetting front is formed, it was proposed by Mudawar et al. [26] that since the wave propagates downstream a short distance before the liquid-vapor interface is lifted from the surface, δ used to determine $\overline{P_f - P_g}$ should be calculated at an axial location of $z = 1.5\ \lambda_c$, which is the average between the location where the first wave front is formed and the location of the first wave peak. For completeness, Table 4 shows the closed form CHF equations for δ calculated at both $z = \lambda_c$ and $z = 1.5\ \lambda_c$ for the two limiting cases where either the interfacial shear or the vapor momentum terms are neglected. Interestingly, the above assumptions produce four closed-form CHF equations that are similar in form to the horizontal upward-facing CHF relation, equation (9), recommended by Kutateladze [52] and Zuber et al. [32].

Table 5 compares CHF values at 90° determined from the four combinations of assumptions indicated in Table 4 to the predictions of the complete iterative numerical scheme. The assumption that $\rho_g'' = \rho_g$ results in CHF predictions 21.0 to 32.5% smaller than CHF solutions where $\rho_g'' = \rho_g \coth(k_c H_g)$. Additionally, when $\rho_g'' = \rho_g$ is utilized to predict CHF at orientations other than vertical, the instability theory predicts stable waves at a much smaller inclination (135°, rather than 161° obtained with the present numerical model).

Mudawar et al. [26] showed that the assumption of negligible shear stress increased the mean vapor velocity by 50% or more, but that the assumption of negligible momentum gradient was justified for large axial locations, with an approximate error of only 5%. However, the error increases to nearly 20% for small axial locations (3–5 mm). Since the mean vapor velocity, $\bar{u}_g$, is taken at a location of $z = \lambda_c$, and λ_c is smaller than 5 mm for all orientations less than 150°, it is suggested that the momentum gradient be retained when attempting to accurately predict CHF orientation effects in the near-vertical region. The full separated flow model utilized in the near-vertical CHF model is described in Appendix A.

8. Conclusions

Saturated pool boiling experiments and flow visualization studies were performed at various heater surface orientations to ascertain the CHF trigger mechanism associated with each orientation. Key conclusions from the study are as follows:

1. Based on the vapor behavior observed just prior to CHF, it was shown that surface orientations can be divided into three regions: upward-facing (0–60°), near-vertical (60–165°) and downward-facing (> 165°). In the upward-facing region, the buoyancy forces remove the vapor vertically off the heater surface. The near-vertical region is characterized by a wavy liquid-vapor interface which sweeps along the heater surface. In the downward-facing region, the vapor repeatedly stratifies on the surface, greatly decreasing CHF.
2. The vast differences between the observed vapor behavior within the three regions indicate that a single overall pool boiling CHF model cannot possibly account for all the observed orientation effects, but instead three different models should be developed for the three regions. This study focused on modeling the near-vertical region, which covers close to 60% of all orientation angles, as determined from photographic evidence presented in this paper.
3. The near-vertical regime was modeled based on the observations that: (i) at high heat flux conditions,

Table 5
FC-72 CHF predictions at (in units of W cm^{-2}) 90° for different near-vertical model assumptions

	δ calculated at $z = 1\ \lambda_c$		δ calculated at $z = 1.5\ \lambda_c$	
Separated flow model assumptions	$\rho_g'' = \rho_g \coth(k_c H_g)$ $H_g = \delta$ at $z = \lambda_c$	$\rho_g'' = \rho_g$	$\rho_g'' = \rho_g \coth(k_c H_g)$ $H_g = \delta$ at $z = \lambda_c$	$\rho_g'' = \rho_g$
Full model	16.24[a]	11.38	19.77	15.21
Neglecting momentum gradient	18.58	12.65	23.51	17.74[b]
Neglecting shear stress	19.78	15.00[c]	22.85	18.16

[a] Solution from present model
[b] Solution presented by Mudawar et al. [26]
[c] Solution presented by Mudawar et al. [53]

near-vertical pool boiling exhibits vapor production and vapor flow patterns similar to those found in flow boiling; (ii) a fairly continuous wavy vapor layer engulfs the heater surface at heat fluxes slightly smaller than CHF; (iii) boiling remains active in the wetting fronts, where the interface of the vapor layer contacts the heater surface; and (iv) CHF is triggered when the normal momentum of the vapor produced in the wetting front exceeds the pressure force exerted upon the interface due to interfacial curvature and the wetting front is lifted from the heater surface. The model shows good agreement with CHF data for different fluids and is also very accurate in predicting the angle of transition between the near-vertical and downward-facing regimes.

Acknowledgements

The authors gratefully acknowledge the support of the Office of Basic Energy Sciences of the U.S. Department of Energy (Grant No. DE-FE02-93ER14394). Financial support for the first author was also provided by the American Association of University Women Educational Foundation through a selected Professions Fellowship.

Appendix A

Separated flow model

Applying mass and energy conservation for a control volume of the vapor layer of length dz, combining the two equations and integrating with respect to z, gives

$$\rho_g \bar{u}_g \delta = \frac{q_m z}{h_{fg}\left[1+\frac{c_{p,f}\Delta T_{sub}}{h_{fg}}\right]}. \quad (A.1)$$

A momentum balance on the same control volume yields

$$\frac{d}{dz}[\rho_g \bar{u}_g^2 \delta] = \delta(\rho_f - \rho_g) g_e \sin\theta - \tau_i \quad (A.2)$$

where interfacial shear stress, τ_i, is defined as $\tau_i = 0.5 f_i \rho_g \bar{u}_g^2$. For the interfacial friction factor, Galloway and Mudawar [45] and Gersey and Mudawar [46] found that a constant value of $f_i = 0.5$ provided the best agreement between measured and predicted pressure drops obtained from flow boiling studies. For vertical pool boiling, a parametric study of f_i ranging from 0.25 to 1.0 indicated that the value of f_i does not significantly affect separated flow model results. Therefore, a value of $f_i = 0.5$ was utilized in the present study as well. The wall interfacial shear stress can also be included in equation (A.2), but was found to be negligible, changing the value of the mean vapor velocity by less than 0.2%.

Combining equations (A.1) and (A.2) produces the following differential equation relating $\bar{u}_g$ to z.

$$\frac{d}{dz}[\bar{u}_g z] = \frac{(\rho_f - \rho_g) g_e \sin\theta}{\rho_g}\frac{z}{\bar{u}_g} - 0.5 f_i \rho_g \bar{u}_g^2 \frac{h_{fg}\left[1+\frac{c_{p,f}\Delta T_{sub}}{h_{fg}}\right]}{q_m} \quad (A.3)$$

where $f_i = 0.5$. Equation (A.3) was solved numerically using a 4th-order Runge–Kutta routine. The stream-wise step size of 0.0001 m provided an accuracy of ± 0.01 m s^{-1} for the velocity solution. The code was verified by solving equation (A.3) both analytically and numerically for the limiting case where the interfacial shear stress is neglected. The numerical results agreed well with the analytical solution.

References

[1] M.S. El-Genk, A. Guo, Transient boiling from inclined and downward-facing surfaces in a saturated pool, International Journal of Refrigeration 6 (1993) 414–422.
[2] S. Ishigai, K. Inoue, Z. Kiwakik, T. Inai, Boiling heat transfer from a flat surface facing downward, Proceedings of the International Heat Transfer Conference, Boulder, CO, 1961, pp. 224–229.
[3] P.M. Githinji, R.H. Sabersky, Some effects of the orientation of the heating surface in nucleate boiling, ASME Journal of Heat Transfer 85 (1963) 379.
[4] R.P. Anderson, L. Bova, The role of downfacing burnout in post-accident heat removal, Transactions of the American Nuclear Society 14 (1971) 294.
[5] D.N. Lyon, Boiling heat transfer and peak nucleate boiling fluxes in saturated liquid helium between the triple point and critical temperature, Advances in Cryogenic Engineering, Vol. 10, No. 2, 1965, pp. 371–379.
[6] Y. Katto, S. Yokoya, M. Yasunaka, Mechanism of boiling crisis and transition boiling in pool boiling, Proceedings of the Fourth International Heat Transfer Conference, Paris–Versailles, Vol. V, B3.2, 1970.
[7] M. Jergel, R. Stevenson, Static heat transfer to liquid helium in open pools and narrow channels, International Journal of Heat and Mass Transfer 14 (1971) 2099–2107.
[8] M. Jergel, R. Stevenson, Heat transfer to boiling helium from aluminum surfaces, Cryogenics 12 (1972) 312–313.
[9] H. Merte Jr., E. Oker, J.W. Littles, Boiling heat transfer to LN2 and LH2: Influence of surface orientation and reduced body forces, Proceedings of the XIIIth International Congress of Refrigeration, Paper 1.62, 1973, pp. 191–196.
[10] L. Bewilogua, R. Knoner, H. Vinzelberg, Heat transfer in cryogenic liquids under pressure, Cryogenics 15 (1975) 121–125.
[11] I.P. Vishnev, I.A. Filatov, Y.G. Vinokur, V.V. Gorokhov, G.G. Svalov, Study of heat transfer in boiling of helium on surfaces with various orientations, Heat Transfer—Soviet Research 8 (3) (1976) 104–108.
[12] V.I. Deev, V.E. Keilin, I.A. Kovalev, A.K. Kondratenko,

V.I. Petrovichev, Nucleate and film pool boiling heat transfer to saturated liquid helium, Cryogenics 17 (1977) 557–562.
[13] I.I. Gogonin, S.S. Kutateladze, Critical heat flux as a function of heater size for a liquid boiling in a large enclosure, Journal of Engineering Physics (Translated from Inzhenerno-Fizicheskii Zhurnal) 33 (1978) 1286–1289.
[14] C. Beduz, R.G. Scurlock, A.J. Sousa, Angular dependence of boiling heat transfer mechanisms in liquid nitrogen, Advances in Cryogenic Engineering 33 (1988) 363–370.
[15] S. Nishio, G.R. Chandratilleke, Steady-state pool boiling heat transfer to saturated liquid helium at atmospheric pressure, JSME International Journal 32 (Series II) (1989) 639–645.
[16] S.M. You, Pool boiling heat transfer with highly-wetting dielectric fluids, Ph.D. Thesis, University of Minnesota, Minneapolis, MN, 1990.
[17] Z. Guo, M.S. El-Genk, An experimental study of saturated pool boiling from downward facing and inclined surfaces, International Journal of Heat and Mass Transfer 35 (1992) 2109–2117.
[18] A.A. Gribov, G.S. Taranov, N.M. Turchin, A.A. Tsyganok, Heat transfer and limiting heat loads in water boiling on downward-facing plane and spherical surfaces, Heat Transfer Research 25 (4) (1993) 754–759.
[19] V.S. Granovskii, A.A. Sulatskii, S.M. Shmelev, The crisis of nucleate boiling on a horizontal surface facing downward, High Temperature 32 (1) (1994) 78–90.
[20] M.J. Brusstar, H. Merte, Effects of buoyancy on the critical heat flux in forced convection, Journal of Thermophysics and Heat Transfer 8 (1994) 322–328.
[21] J.Y. Chang, S.M. You, Heater orientation effects on pool boiling of micro-porous-enhanced surfaces in saturated FC-72, ASME Journal of Heat Transfer 118 (1996) 937–943.
[22] S.J. Reed, Elimination of boiling incipience temperature drop and enhancement of boiling heat transfer in highly wetting fluids through low contact force attachments, Master's Thesis, Purdue University, West Lafayette, IN, 1996.
[23] S.J. Reed, I. Mudawar, Enhancement of boiling heat transfer using highly wetting liquids with pressed-on fins at low contact forces, International Journal of Heat and Mass Transfer 40 (1997) 2379–2392.
[24] T.Y. Chu, B.L. Bainbridge, R.B. Simpson, J.H. Bentz, Ex-vessel boiling experiments: laboratory and reactor scale testing of the flooded cavity concept for in-vessel core retention Part I: observations of quenching of downward-facing surfaces, Nuclear Engineering and Design 169 (1997) 77–88.
[25] S.H. Yang, W.P. Baek, S.H. Chang, Pool boiling critical heat flux of water on small plates: effects of surface orientation and size, International Communications in Heat and Mass Transfer 24 (1997) 1093–1102.
[26] I. Mudawar, A.H. Howard, C.O. Gersey, An analytical model for near-saturated pool boiling critical heat flux on vertical surfaces, International Journal of Heat and Mass Transfer 40 (1997) 2327–2339.
[27] M.J. Brusstar, H. Merte, R.B. Keller, B.J. Kirby, Effects of heater surface orientation on the critical heat flux—I. An experimental evaluation of models for subcooled pool boiling, International Journal of Heat and Mass Transfer 40 (1997) 4007–4019.
[28] I.P. Vishnev, Effect of orienting the hot surface with respect to the gravitational field on the critical nucleate boiling of a liquid, Journal of Engineering Physics (Translated from Inzhenerno-Fizicheskii Zhurnal) 24 (1974) 43–48.
[29] M.J. Brusstar, H. Merte, Effects of heater surface orientation on the critical heat flux—II. A model for pool and forced convection subcooled boiling, International Journal of Heat and Mass Transfer 40 (1997) 4021–4030.
[30] J.H. Lienhard, V.K. Dhir, Hydrodynamic prediction of peak pool-boiling heat fluxes from finite bodies, ASME Journal of Heat Transfer 95 (1973) 477–482.
[31] R.J. Moffat, Describing the uncertainties in experimental results, Experimental Thermal and Fluid Science 1 (1988) 3–17.
[32] N. Zuber, M. Tribus, J.W. Westwater, The hydrodynamic crisis in pool boiling of saturated and subcooled liquids, International Developments in Heat Transfer: Proceedings of the 1961–62 International Heat Transfer Conference, Boulder, CO, 1961, pp. 230–236.
[33] Y. Haramura, Y. Katto, A new hydrodynamic model of critical heat flux, applicable widely to both pool and forced convection boiling on submerged bodies in saturated liquids, International Journal of Heat and Mass Transfer 26 (1983) 389–399.
[34] R.F. Gaertner, Photographic study of nucleate pool boiling on a horizontal surface, ASME Journal of Heat Transfer 87 (1965) 17–29.
[35] Y. Katto, S. Yokoya, Principal mechanism of boiling crisis in pool boiling, International Journal of Heat and Mass Transfer 11 (1968) 993–1002.
[36] Y. Katto, S. Yokoya, Behavior of a vapor mass in saturated nucleate and transition pool boiling, Heat Transfer—Japanese Research 5 (1) (1976) 45–65.
[37] J.H. Lienhard, Things we don't know about boiling heat transfer: 1988, International Communications in Heat and Mass Transfer 15 (1988) 401–428.
[38] Y. Katto, Critical heat flux in pool boiling, in: V.K. Dhir, A.E. Bergles (Eds.), Pool and External Flow Boiling, ASME, New York, 1992, pp. 151–164.
[39] A.E. Bergles, What is the real mechanism of CHF in pool boiling? in: V.K. Dhir, A.E. Bergles (Eds.), Pool and External Flow Boiling, ASME, New York, 1992, pp. 165–170.
[40] M.P. Fiori, A.E. Bergles, Model of critical heat flux in subcooled flow boiling, Proceedings of the Fourth International Heat Transfer Conference, Paris-Versailles, France, Vol. VI, 1970, pp. 354–365.
[41] R. Hino, T. Ueda, Studies on heat transfer and flow characteristics in subcooled flow boiling—part 1. Boiling characteristics, International Journal of Multiphase Flow 11 (1985) 269–281.
[42] R. Hino, T. Ueda, Studies on heat transfer and flow characteristics in subcooled flow boiling—part 2. Flow characteristics, International Journal of Multiphase Flow 11 (1985) 283–297.
[43] J.E. Galloway, I. Mudawar, CHF mechanism in flow boiling from a short heated wall—I. Examination of near-wall conditions with the aid of photomicrography and high speed video imaging, International Journal of Heat and Mass Transfer 36 (1993) 2511–2526.
[44] C.O. Gersey, I. Mudawar, Effects of heater length and orientation on the trigger mechanism for flow boiling

CHF—I. Photographic study and statistical characterization of the near-wall interfacial features, International Journal of Heat and Mass Transfer 38 (1995) 629–641.
[45] J.E. Galloway, I. Mudawar, CHF mechanism in flow boiling from a short heated wall—II. Theoretical CHF model, International Journal of Heat and Mass Transfer 36 (1993) 2527–2540.
[46] C.O. Gersey, I. Mudawar, Effects of heater length and orientation on the trigger mechanism for flow boiling CHF—II. CHF model, International Journal of Heat and Mass Transfer 38 (1995) 643–654.
[47] J.C. Sturgis, I. Mudawar, Critical heat flux in a long, rectangular channel subjected to one-sided heating—I. Flow visualization, International Journal of Heat and Mass Transfer, in press.
[48] J.C. Sturgis, I. Mudawar, Critical heat flux in a long, rectangular channel subjected to one-sided heating—II. Analysis of CHF data, International Journal of Heat and Mass Transfer, in press.
[49] H. Lamb, Hydrodynamics, 6th ed., Dover Publications, New York, 1945.
[50] L.M. Milne-Thompson, Theoretical Hydrodynamics, 4th ed., Macmillan, New York, 1960.
[51] J.E. Galloway, I. Mudawar, A theoretical model for flow boiling CHF from short concave heaters, ASME Journal of Heat Transfer 117 (1995) 698–707.
[52] S.S. Kutateladze, On the transition to film boiling under natural convection, Kotloturbostroenie 3 (1948) 10–12.
[53] I. Mudawar, J.E. Galloway, C.O. Gersey, S.J. Reed, Theoretical modeling of CHF for near-saturated pool boiling and flow boiling from short heaters using the interfacial lift-off criterion, in: J.C. Chen, Y. Fujita, F. Mayinger, R.A. Nelson (Eds.) Convection Flow Boiling, Taylor and Francis, Washington, DC, 1996, pp. 345–350.